Simultaneous classification and location of volcanic deformation in SAR interferograms using a convolutional neural network

M. Gaddes[1], A. Hooper[1], F. Albino[2],

[1]COMET, University of Leeds, UK.

[2]School of Earth Sciences, University of Bristol, UK.

Key Points:

- The three channels of pretrained CNNs cannot be used with different InSAR data (e.g. phase and DEM).
- Our VolcNet database of InSAR time series contains up to ~500,000 labelled interferograms.
- Our CNN uses unwrapped data to differentiate between deformation patterns, and determines their size.

Corresponding author: M. Gaddes, m.e.gaddes@leeds.ac.uk

Abstract

This manuscript is an EarthArXiv preprint that has been submitted to Journal of Geophysical Research: Solid Earth. It has previously undergone peer review with Remote Sensing of Environment, but was deemed outside the remit of the journal.

With the evolution of InSAR into a tool for active hazard monitoring, new methods are sought to quickly and automatically interpret the large number of interferograms that are created. We present a convolutional neural network (CNN) that is able to both classify the type of deformation, and to locate the deformation within an interferogram in a single step. We achieve this through building a "two headed model", which returns both outputs after one forward pass of an interferogram though the network. We train our model by first creating a dataset of synthetic interferograms, but find that our model's performance is improved through the inclusion of real Sentinel-1 data. When building models of this type, it is common for some of the weights within the model to be transferred from other models designed for different problems. Consequently, we also investigate how to best organise interferograms such that the filters learned in other domains are sensitive to the signals in interferograms, but find that using different data in each of the three input channels degrades performance when compared to the simple case of repeating wrapped or unwrapped phase across each channel. We also release our labelled Sentinel-1 interferograms as a database named VolcNet, which consists of $\sim$500,000 labelled interferograms. VolcNet comprises of time series of unwrapped phase and labels of the magnitude, location, and duration of deformation, which allows for the automatic creation of interferograms between any two acquisitions, and greatly increases the amount of data available compared to other labelling strategies.

1 Introduction

In recent years, work to extend volcano monitoring to all of the world's $\sim$1400 subaerial volcanoes has resulted in the application of several machine learning methods to ground deformation maps produced by interferometric synthetic aperture radar (InSAR). Convolutional neural networks (CNNs) have been used in *Anantrasirichai et al.* [2018, 2019a] and *Valade et al.* [2019] to determine if individual interferograms contain deformation. This approach has been extended, through using cumulative time series, to more subtle deformation signals that are not visible in a single short temporal baseline Sentinel-

1 interferogram [*Anantrasirichai et al.*, 2019b]. Time series have been used by *Sun et al.* [2020] to detect subtle deformation, with independent component analysis (ICA) by *Gaddes et al.* [2018] to detect signs of unrest relative to a baseline stage of a volcano's behaviour, and with the CUSUM algorithm by *Albino et al.* [2020] to detect signs of unrest. However, in all of the examples detailed above, each algorithm demonstrates very limited knowledge of the diverse types of deformation that may be measured at volcanoes. The algorithm presented in *Anantrasirichai et al.* [2019a] assigns all data containing deformation to one label, whilst the algorithms presented in *Gaddes et al.* [2018] and *Albino et al.* [2020] alerts users to changes in the signals present, but does not identify the type of deformation present. Consequently, we seek to improve upon these approaches by developing a CNN that is able to differentiate between different types of deformation, and to detect the spatial extent of it.

Figure 1A shows the hierarchy of computer vision object/signal identification methods. The algorithm presented in *Anantrasirichai et al.* [2018] contains a model that performs classification and, by breaking larger images into smaller tiles that are each classified, the algorithm as a whole is able to perform localisation. This approach has the limitation that the deep learning model used in this algorithm does not need to learn how to determine the location or size of the object (or signal) of interest, and at a more fundamental level, remains a classification and not localisation model. However, in the field of computer vision, CNNs have been developed that are able to perform both classification and localisation on images that contain either single or multiple objects. The location of an object is either indicated through encompassing it in a rectangle (e.g. localisation or object detection, *Simonyan and Zisserman* [2014]; *Redmon et al.* [2016]) or, in more complex algorithms, indicating the exact outline of an object by identifying which pixels comprise it (e.g. instance segmentation, *He et al.* [2017]). These approaches should provide more detailed information on the spatial extent of a signal of interest than a classification model that is repeatedly used on different areas of the representation. Consequently, we endeavour to advance the state of the art through developing a CNN that is able to both localise deformation within an interferogram, and to classify different types of deformation (the hierarchy of which we show in Figure 1B).

When constructing a CNN to perform both classification and localisation with data derived from SAR satellites, a new CNN could be designed before all the parameters within it are trained. However, this approach has the risk of failing to utilise both the successful structures and the learned parameters of CNNs that have been successfully applied to other computer vision problems (e.g. the classification of natural images in *Krizhevsky et al.* [2012] and *Simonyan and Zisserman* [2014], the instance segmentation of biomedical images in *Ronneberger et al.* [2015], or the detection of buildings in satellite imagery in *Zhang et al.* [2016]). In order to describe how we can utilize these successes, we must first introduce the structure of a CNN in more detail, which we do with the use of Figure 1C. In this figure, a CNN can be seen to comprise of a convolutional part, and a fully connected part. The convolutional part comprises of filters that are convolved across an image to extract deep representations, whilst downsampling is performed simultaneously to reduce the spatial size of the features as their depth increases. In the case of the example network shown in Figure 1C, a three channel (colour) image of size $(224 \times 224 \times 3)$ pixels is transformed into a spatially smaller but deep $(7 \times 7 \times 512)$ representation by this process. In the second part, this 3D representation is flattened into a vector (which in this example would be of size $(7 \times 7 \times 512 = 25088)$), before a traditional neural network comprising of interconnected neurons is used to create the desired model outputs. The size of the last layer of this second part is dependent on features such as the number of different classes present in the data and, in this example case with two neurons in the last layer, would be used in a case in which there were only two different classes.

Consequently, when using an existing model on a new problem, any change in the number or type of output classes will require changing the fully connected part of the network. Therefore, it is common to retain the structure of the convolutional layers (i.e. part one of the model) and design a new fully connected network (i.e. part two of the model) that outputs the classes required by the new problem. However, this approach still requires the training of a CNN that is likely to contain tens of millions of parameters, which will be both computationally expensive, and require a large volume of training data. AlexNet, a previously state-of-the-art image classification CNN (named after one of the designers, Alex Krizhevsky), has 60 million parameters, was trained on 1.2 million images, and even when implemented on GPUs took around one week to train [*Krizhevsky et al.*, 2012]. Therefore, a common approach termed transfer learning is to retain both the structure and weights of the initial convolutional layers, and to train only the fully connected part of the network.

The weights learned in the convolutional filters of a CNN are of great importance to a network's ability to detect features, as the filters must be sensitive to the patterns that these features present in an image. As networks such as AlexNet [*Krizhevsky et al.*, 2012] and VGG16 (*Simonyan and Zisserman* [2014], named after the University of Oxford Visual Geometry Group) were originally developed to compete in the ImageNet competitions [*Deng et al.*, 2009], the filters have been trained to detect the type of features present in natural images (e.g. photographs of a person, or car). When performing transfer learning, it is these filters that must be sensitive to the patterns presented in a deformation signal if the network is to correctly classify and locate it. However, as interferograms can be expressed in differing formats we also seek to explore which of these formats allows for the filters in models trained on natural images to excel.

2 Classification with different data formats

As the most common CNNs for computer vision are trained on images comprising of a channel for each of the red, green, and blue values for each pixel, other data that are to be used with the network would also ideally be three channel. However, when considering an image of interferometric phase, these images contain only a single value for each pixel, and so consist of only one channel. This difference in the number of channels can be circumvented through duplicating the one channel interferogram in each of the three input channels of a CNN, or by discarding parts of the filters of the first convolution (e.g. a filter of size $(5 \times 5 \times 3)$ be reduced to $(5 \times 5 \times 1)$). However, in this section of our study we wish to determine if this approach can be improved upon by utilising the three channel structure of many pre-trained CNNs to input more data to the model.

When two SAR images are combined to form a single interferogram, the resulting image is a $2D$ array of complex numbers [*Hanssen*, 2001]. Whilst the magnitude of each of these complex numbers relates to the underlying brightness and coherence of a given pixel, it is common for only the argument to be displayed, as these phase values can be used to infer ground movement. However, the phase values of an interferogram are wrapped in the range $[-\pi, \pi]$ as only the fractional part of the phase value can be measured, but this ambiguity can be estimated to produce an unwrapped interferogram [*Chen and Zebker*, 2001]. We postulate that in addition to the use of either wrapped or unwrapped data duplicated to fill three channels, the original complex numbers of an interferogram could be used in two channels, and so allow the network to use interferometric amplitude as an indicator of the reliability of the phase.

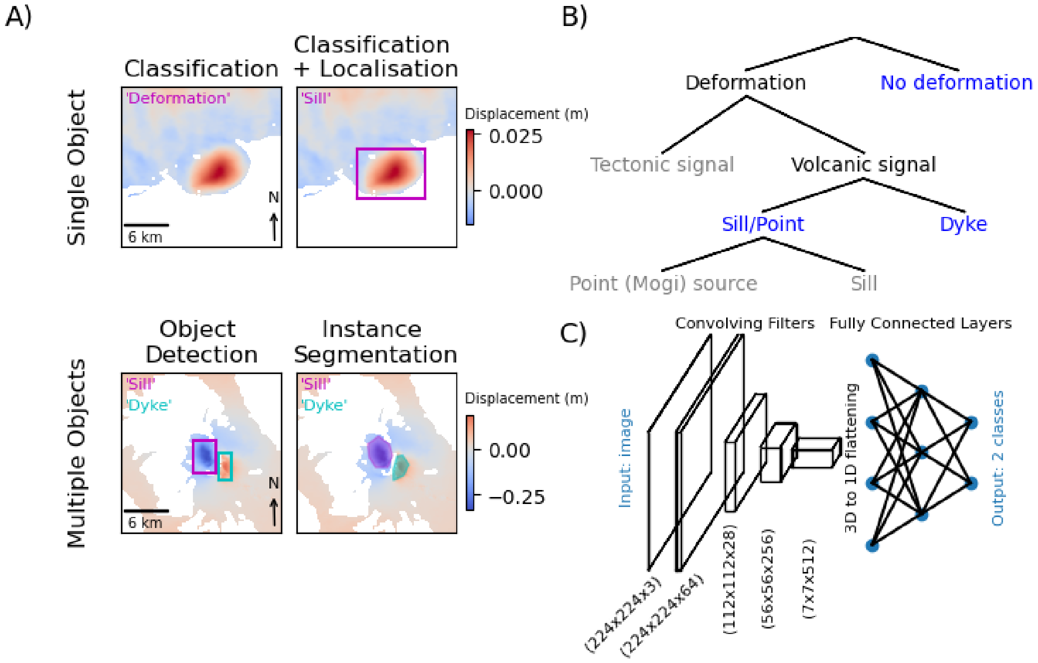

Figure 1. A) Introduction to the hierarchy of computer vision object/signal identification methods. The upper and lower rows show 12 day descending Sentinel-1 interferograms of Sierra Negra and Wolf volcano (Galapagos Archipelago, Ecuador), respectively. The Sierra Negra interferogram contains only one signal (an inflating sill), whilst the Wolf interferogram contains two signals (a deflating sill and an opening dyke). B) Proposed hierarchy for signals of interest in interferograms at volcanic centres. We propose a model that is able to classify interferograms into one of the three classes shown in blue: "no deformation", "Dyke", and ""Sill/Point". We envisage that future studies may add further classes which we mark in grey, such as those that differentiate between sills and point sources. C) Overview of a traditional convolutional neural network (CNN), showing how convolving filters and downsampling create a small but deep representation of an image ($(224 \times 224 \times 3)$ to $(7 \times 7 \times 512)$), which is then flattened and passed through a traditional neural network.

However, we can also consider external data to feed into the CNN. When a human observer interprets an interferogram, they are likely to use data such as a digital elevation model (DEM) as this can be used to help determine if a signal is due to deformation, or due to a topographically-correlated atmospheric phase screen. This problem is of particular importance at stratovolcanoes, as the cones typical of these volcanoes can be several kilometres high, and therefore be capable of creating large and spatially stationary signals in interferograms. The body of literature that covers the application of InSAR to volcanic deformation is replete with studies that consider which of the two mechanisms are responsible for the observed signals, and examples include *Beauducel et al.* [2000]; *Rémy et al.* [2015]; *Yip et al.* [2019]. When considering previous attempts at the automatic detection of deformation signals in Sentinel-1 interferograms, *Anantrasirichai et al.* [2019a] also reported that many of the false positives recovered by their algorithm were caused by signals correlated with topography. Consequently, we postulate that the inclusion of a DEM in the inputs to our CNN will improve its ability to differentiate between deformation signals and atmospheric signals that are correlated with topography, and therefore seek to investigate its use as an input into a multichannel model.

To perform this analysis, we first synthesise a dataset of labelled interferograms. To achieve this, we have created an open source Python3 package named SyInterferoPy, which we make freely available to the community via GitHub: (https://github.com/matthew-gaddes/SyInterferoPy). The collection of enough labelled data to train a CNN is commonly time consuming or expensive, and we find that the addition of localisation labels to our data makes it more time consuming than in previous studies. Additionally, due to the large number of data that are required to train CNNs and our expansion to classification of different types of deformation, procuring enough real data to do this may not be possible. Consequently, we perform this analysis using only synthetic data. Following the hierarchy proposed in Figure 1B, we create interferograms that contain either no deformation, deformation due to an opening dyke, or deformation due to a sill or point source. These sources were chosen after reviewing the database of volcanic deformation events measured using InSAR in *Biggs et al.* [2014] as we believe they cover the majority of the observed signals that are of importance for volcano monitoring (i.e. we disregard signals due to processes such as the cooling of lava flows). Model parameters were chosen to be both physically realistic (e.g. dykes have near vertical dips), and for the resulting deformation patterns to have absolute magnitudes in the range $[0.05, 0.3]$ m which ensured that the signals are visible over the synthetic atmospheric signals. We model the dykes as vertical dislocations with uniform opening in an elastic half space [*Okada*, 1985] with strikes in the range $[0, 359°]$, dips in the range $[75, 90°]$, openings in the range $[0.1, 0.7]$ m, top depths in the range $[0, 2]$ km, bottom depths in the range $[0, 8]$ km, and lengths in the range $[0, 10]$ km. We model the sill/point sources as horizontal dislocations with uniform opening in an elastic half space [*Okada*, 1985] with strikes in the range $[0, 359°]$, dips in the range $[0, 5°]$, openings in the range $[0.2, 1]$ m, depths in the range $[1.5, 3.5]$ km, and widths and lengths in the range $[2, 6]$ km. It should be noted that our proposed hierarchy of volcanic deformation signals also includes processes that could be modelled as a point pressure source (commonly referred to as a "Mogi" source [*Mogi*, 1958]) within the sill/point category, but given that we do not envisage that a deep learning model using satellite data from only one look angle (i.e. ascending or descending) would be able to differentiate between these two models, we generate our synthetic data using only one of them for simplicity.

These deformation patterns are then combined with a topographically correlated atmospheric phase screen (APS), and a turbulent APS, which we discuss generating in more detail in *Gaddes et al.* [2018]. We calculate the topographically correlated APS using the Shuttle Radar Topography Mission (SRTM) 90m DEM [*Farr et al.*, 2007], and use the coastline information contained within the product to mask areas of water. We also synthesise areas of incoherence within our interferograms, which we mask in order for our synthetic interferograms to be as similar as possible to the Sentinel-1 interferograms automatically created by the LiCSAR processor [*Lazeckỳ et al.*, 2020]. Figure 2 shows the results of mixing these different elements to create our synthetic interferograms, and the range of sizes of deforming regions that the different deformation model parameters produce (e.g. Interferogram 2 versus Interferogram 3).

This process creates unwrapped data, which can be converted to wrapped data through finding modulo 2π of the unwrapped phase. However, to synthesise both the real and imaginary part of a complex interferogram requires knowledge of both the brightness of a pixel and its phase. To achieve this, we again use the SRTM DEM, and calculate the intensity of reflected electromagnetic radiation at the angles of incidence used by the Sentinel-1 satellites $(29.1 - 46.0°)$, before adding speckle noise, and calculating the interferometric amplitude between two images (i.e. the product of the two amplitudes). As inputs to CNNs that are to be trained using transfer learning must be rescaled to the inputs used in the original training data, we use only relative values in the range $[(-1), 1]$ for the synthetic intensities. With knowledge of the modulus (relative intensity) and argument (wrapped phase) of each pixel of our synthetic interferogram, the real/imaginary components are simply the products of the modulus and cosine/sine of the argument, respectively. Figure 3 shows five different ways we can represent an interferogram using the three channels available. Whilst this is not an exhaustive list of possible combinations or data sources, we believe that these five types are able to fully explore our hypothesis on the use of three channel data, yet are not so numerous as to be too computationally expensive to train.

The CNN we build to classify the synthetic interferograms uses the five convolutional blocks of VGG16 [*Simonyan and Zisserman*, 2014], with our own fully connected network after this. This network was chosen as, when used in the field of computer vision for classifying natural images, it outperformed older models such as AlexNet [*Simonyan and Zisserman*, 2014], which is used in the algorithm presented in *Anantrasirichai et al.* [2018], yet remains relatively simple to work with and train when compared to even newer models such as ResNet [*He et al.*, 2016], and Inception [*Szegedy et al.*, 2015]. Additionally, VGG16 was used by *Simonyan and Zisserman* [2014] to perform localisation of items it classifies, and therefore aligns with our goals. Figure 4B shows an overview of the model, in which interferograms of shape $(224 \times 224 \times 3)$ are passed through the five convolutional blocks of VGG16 to create a tensor of shape $(7\times7\times512)$. This is flattened to make a vector of size $25,088$, before being passed through fully connected layers of size 256, 128, and an output layer of size three (i.e., dyke, sill/point, or no deformation). The localisation output shown in the figure is not used in our preliminary exploration of which channel format to use (Section 2), but is used in Section 3. To produce a set of outputs that can be used as probabilities, we use a softmax activation for the last layer [*Bridle*, 1990], but on the remaining layers we use rectified linear units (ReLus) to reduce computation time [*Agostinelli et al.*, 2014]. As our model seeks to solve a classification problem, we use categorical cross entropy for the loss function, which we seek to reduce using the Nadam optimizer as this does not require the choice of a learning rate [*Dozat*, 2016].

To train the model using the five different types of synthetic data, we perform what is termed “bottleneck learning” in machine learning literature (e.g. *Yu and Seltzer* [2011]). This method of training a CNN is used when only the weights within the fully connected layer are updated (i.e. transfer learning is being performed on the convolutional filters), and comprises of first computing the results from passing our entire dataset through the first five blocks of VGG16, before then training only the fully connected parts of our network (i.e. the classification output). When a three channel image is passed through the first five blocks of VGG16, a tensor of shape $(7 \times 7 \times 512)$ and termed a bottleneck feature is created, which we illustrate in Figure 4A. This method is highly efficient as we do not generally wish to update the weights in the convolutional blocks of VGG16, yet passing the data through these blocks is computationally expensive. By passing the data through the convolutional blocks just once, we can then repeat only the relatively inexpensive passes of the data through the fully connected parts of our network as we update the weights contained within these layers. This method is of particular use for practitioners who do not have access to high power computing facilities or GPUs.

A common problem of CNNs that are used for classification can be overfitting of the training data, which results in a model that generalises to new data poorly [*Krizhevsky et al.*, 2012]. Overfitting is commonly caused by insufficient training data, but can also be caused by issues such as using a model with too much complexity for the desired task, or training a model for too many epochs [*Chollet*, 2017]. We endeavour to limit overfitting through the use of dropout [*Srivastava et al.*, 2014] before both the 256 and 128 neuron layers, as through randomly removing some connections during each pass of the data through our model, this method aims to ensure that our model is forced to learn more robust representations of the training data. As we use synthetic data, we are not limited by the usual cost of collecting labelled data, and therefore are able to generate 20000 unique interferograms that are evenly distributed between classes without the use of data augmentation.

Figure 5 shows the results of training five models with each of the data formats previously discussed. The highest classification accuracy achieved is ~0.95, which is achieved when the models are trained with either wrapped or unwrapped data repeated across the three input channels. However, it should be noted that the accuracy of the unwrapped phase model takes the full 20 epochs to achieve this performance, which contrasts with the wrapped phase model which shows little change after the eighth epoch. Inclusion of the DEM as the third channel appears to reduce classification accuracy, whilst very low accuracies are achieved in the real and imaginary channel case. We discuss these results in more detail in Section 4, but for the remainder of the paper we choose to work with data that is unwrapped and repeated across the three input channels. We choose this ap-

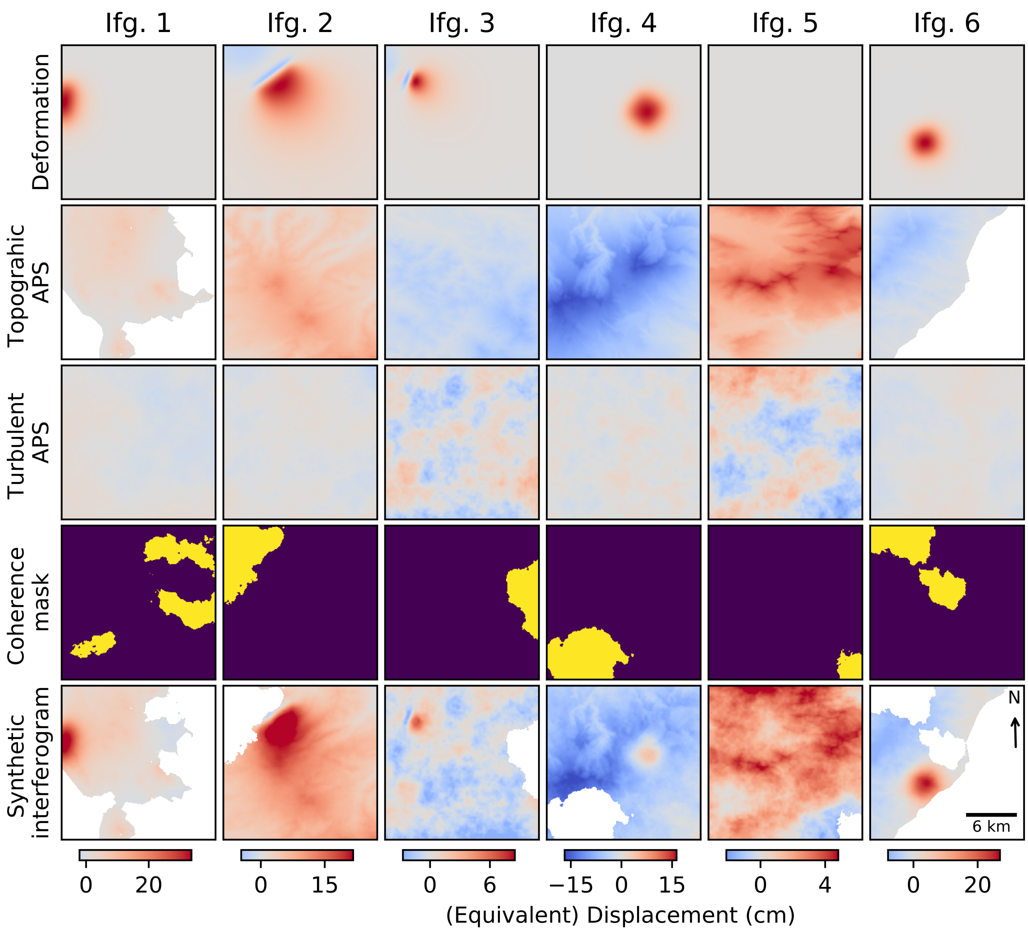

Figure 2. An example of the constituent parts of seven synthetic interferograms. Interferogram 5 does not feature deformation, interferograms 1, 4, and 6 feature deformation due to an sill/point source , and interferograms 2 – 3 feature deformation due to an opening dyke. These signals are geocoded and areas of water masked, before being combined with a topographically correlated APS, and a turbulent APS. Areas of incoherence are also synthesised, and these are used to mask the combination of the three signals to create the final synthetic interferograms.

proach as no significant differences are seen between the classification accuracy ultimately achieved with either wrapped or unwrapped data, but the use of unwrapped data may allow for a model to be used with unwrapped time series, and so detect subtle signals produced by low strain rate processes. Additionally, a model that works with unwrapped data may also provide the opportunity to be expanded to locate and classify unwrapping errors automatically.

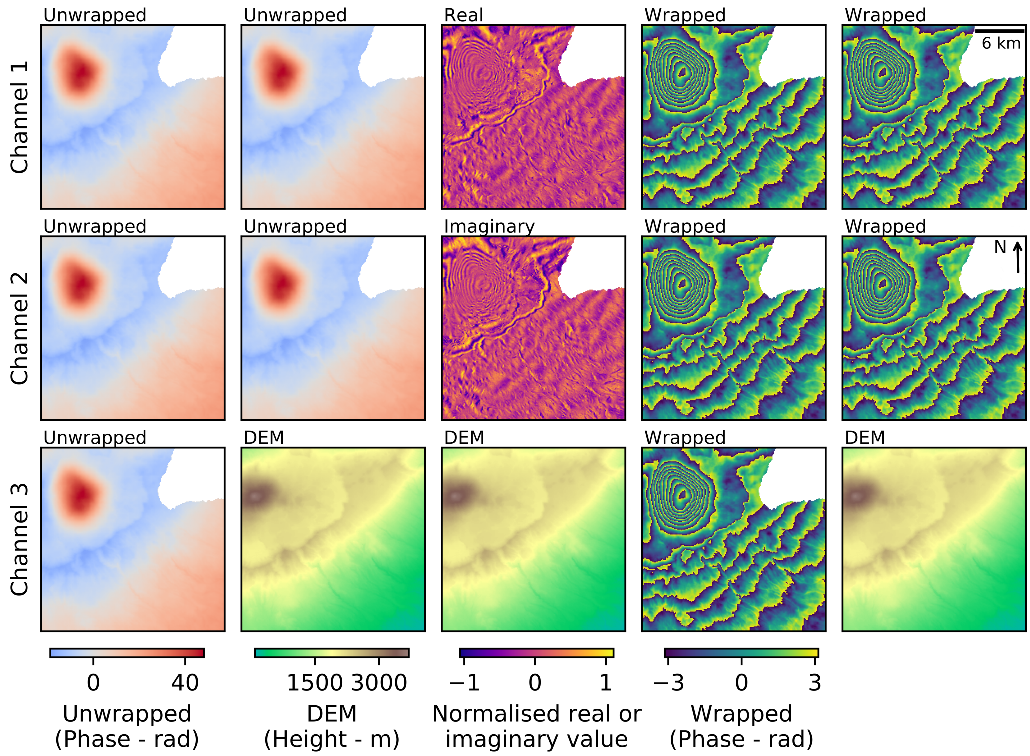

Figure 3. Organisation of an interferogram into three channel form. Columns one and two feature unwrapped data that is repeated, and in column two the DEM is included as the third channel. In column three the real and imaginary elements of the complex values of each pixel of an interferogram occupy channels one and two, whilst the DEM is included in the third. Columns three and four feature wrapped data that is repeated, and in column five the DEM is included as the third channel.

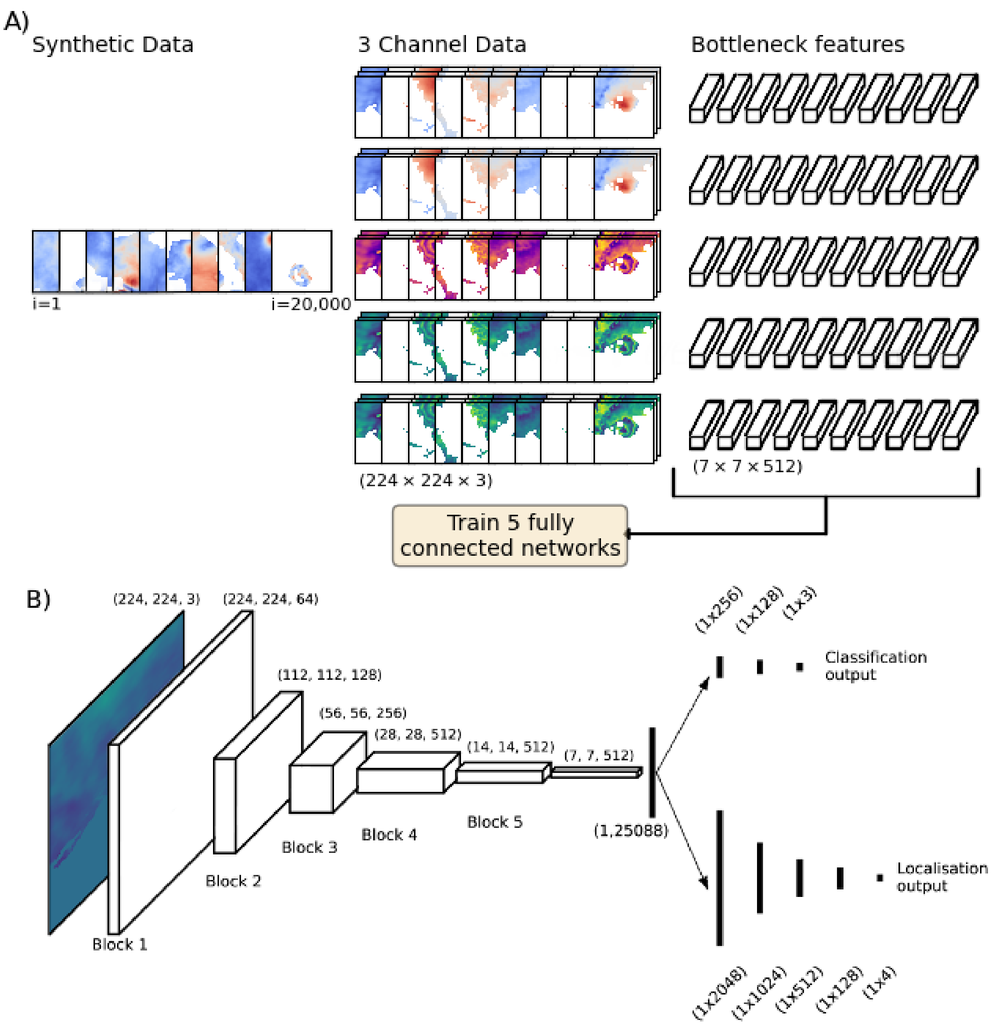

Figure 4. A) Overview of our approach to creating a dataset of synthetic interferograms, arranging these into the five different three channel formats, computing the bottleneck features for each piece of data, and training the fully connected layers of a CNN B)Structure of our classification and localisation CNN. Input interferograms are first passed through the first five convolutional blocks of VGG16 to transform them from size (224 × 224 × 3) to size (7 × 512). These are flattened to create a large fully connected layer featuring 25088 neurons, which is connected to both the upper branch/head, which performs classification, and the lower branch/head, which performs localisation. We find the localisation problem more complex than classification, and consequentially our localisation branch/head features more layers, each with more neurons. The output of the localisation head is a vector of four values determining the position and size of the deformation, whilst the output of the classification head is a vector of three values that indicate the probability for each class, and sum to one.

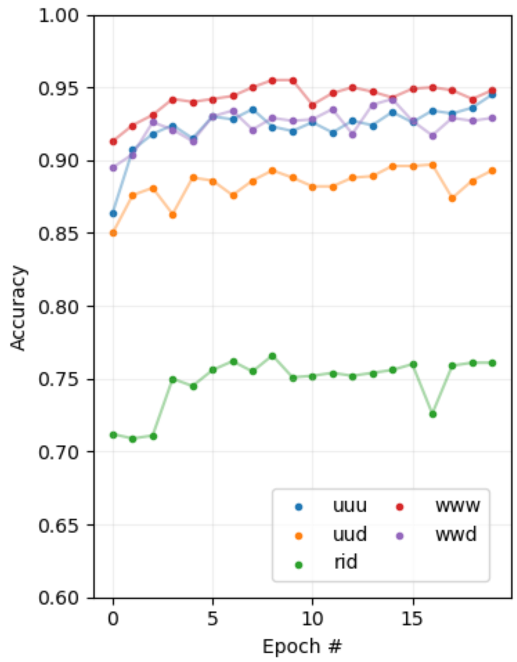

Figure 5. Accuracy of classifying validation data (10% of the total) during training using three channel data arranged in different formats. "u": unwrapped data, "w": wrapped data, "d": DEM, "r" real component of interferogram, "i": imaginary component of interferogram. Low accuracy is seen for the "rid" data, and in both the wrapped and unwrapped cases inclusion of the DEM in the third channel is seen to degrade classification accuracy. At the end of the 20 epochs of training, only a small difference is seen in accuracy between wrapped and unwrapped data, with both classifying ~95% of the validation data correctly, though the wrapped phase model is seen to achieve this level of accuracy more quickly (requiring only eight epochs of training). Whilst we see slight changes in the accuracy at the end of each of the latter epochs, we interpret the lines as having broadly plateaued and conclude that 20 epochs were sufficient for training these models.

3 Classification and localisation

3.1 Using synthetic data

In the previous section, we demonstrated that, when using VGG16 with convolutional weights learned on ImageNet data, roughly optimal performance for classifying synthetic interferograms is achieved when either the wrapped or unwrapped phase is repeated across the three input channels. We choose to progress with only the unwrapped phase model, as the computational cost of unwrapping is often already met by automatic processing systems (e.g. LiCSAR, *Lazeckỳ et al.* [2020]), and the development of models that use unwrapped phase may lead to benefits such as the ability to classify and locate unwrapping errors. In this section, we build on the model used to perform classification by adding localisation output. We also endeavour to ascertain if the expense of collecting labelled data can be avoided entirely through the continued use of synthetic data when training our model.

We achieve both classification and localisation through dividing the fully connected section of our model to produce two distinct outputs. One output returns the class of the input data in the manner described in Section 2, whilst the second returns the location and size of any deformation within the scene. In machine learning parlance, models of this type are termed double headed, and we subsequently refer to either of the outputs and their corresponding preceding layers as either the classification head or localisation head. Figure 4B shows the structure of the two heads, and how they diverge after the output of the fifth block of VGG16 has been flattened. The localisation head is structured in a similar manner to the model described in *Simonyan and Zisserman* [2014], in which the model conveys the location of any deformation through outputting a column vector containing four values. Two of these values determine the centre of the deformation pattern and two display its horizontal and vertical extent. Together, these four values can be used to construct a box encompassing a deformation pattern. However, we find that an acceptable level of localisation performance cannot be achieved with a fully connected network with the same complexity as the classification head, and were required to increase both the number and size of layers in the localisation head's fully connected network. A simple network architecture search finds that the simplest model capable of achieving good performance has five layers consisting of 2048, 1024, 512, 128, and 4 neurons.

We use the mean squared error between the predicted location vector and the labelled location vector as our localisation loss function, which we seek to minimise. When using three arc second pixels (~90m) with a loss function of this type, a mean square error of 400 pixels would correspond to the localisation being incorrect by around $\sqrt{400} = 20$ pixels, or ~2km. However, when using a double headed network, training is complicated by the fact that the model's overall loss is now a combination of the classification and localisation loss, which must be balanced using a hyperparameter commonly termed loss weighting [*Chollet*, 2017]. In contrast to the localisation loss, we use categorical cross-entropy for the classification loss and, as the value produced by this is generally several orders of magnitude lower than the localisation loss, we find that a weighting of 1000 for the classification loss and 1 for the localisation loss produces a model which trains well as the losses are approximately balanced.

To increase the performance of our classification and localisation model, we train it using a two step process. In the first, we train it in a similar manner to that described in the previous section, and update only the parameters within the fully connected network. In the second step, we unfreeze the parameters in the fifth block (i.e. the last convolutional filters of VGG16), and continue to train both these parameters and those contained within the fully connected network. As the second step starts with parameters that are already approximately correct, optimizers that adaptively change the learning rate cannot be used, as any initial large updates can destroy a model's performance. Instead, we use the "Adam" optimizer [*Kingma and Ba*, 2014] and, after experimentation, find a learning rate of 1×10^{-5} neither destroys previous model performance, nor is too slow to train. As the updates to the fifth block performed in the second step of our training preclude the use of bottleneck features, we instead train our classification and localisation model on a Nvidia GTX 1070 GPU.

3.2 Application to real data: the VolcNet database

Whilst the model described in the previous section achieved good performance when classifying and locating deformation in synthetic interferograms, for use in automatic detection algorithms we require our CNN to work with Sentinel-1 data. These data are of particular importance for volcano monitoring, as the European Space Agency's data policy ensures that Sentinel-1 data are available quickly and at no cost, whilst the low revisit times ensure that the majority of sub-aerial volcanoes are imaged at least every 12 days.

We therefore create a database of labelled Sentinel-1 interferograms, which we term VolcNet and make freely available via GitHub: https://github.com/matthew-gaddes/VolcNet

To populate our database, we chose a selection of volcanoes for which deformation is known, and which the LiCSAR automatic interferogram processor (https://comet.nerc.ac.uk/COMET-LiCS-portal/) had created networks of interferograms with no gaps and of long temporal duration (e.g. multiple years). This resulted in our use of Campi Flegrei, Vesuvius, Agung, Wolf, Sierra Negra, Cerro Azul, Erta Ale, La Palma, and Domuyo. We filtered the interferograms with a Goldstein filter [*Goldstein and Werner*, 1998], unwrapped using SNAPHU [*Chen and Zebker*, 2001], and masked pixels with an average coherence below 0.7, before creating time series using LiCSBAS [*Morishita et al.*, 2020].

To label our database, we develop an approach in which we create generic labels that describe the duration, magnitude, and spatial extent of deformation for each volcano. In contrast to traditional labelling approaches that assign a label to individual interferograms (e.g. for InSAR data, *Anantrasirichai et al.* [2018] and *Bountos et al.* [2022]), our approach allows us to create labelled interferograms between any two Sentinel-1 acquisitions. Consequently, with relatively few labels, time series with N acquisitions can be quickly converted into sets of $N^2 - N$ labelled interferograms. We define two types of deformation label: transient deformation, which is relatively short lived and would be imaged by a syneruptive interferogram, and persistent deformation, which is generally of low rate but spans multiple acquisitions. A choice of threshold is also required for the deformation predicted by the label to be considered as visible in an interferogram, as in the cases of persistent deformation of low-rate, we do not want our short temporal baseline interferograms (e.g. 12 days) to be labelled as containing deformation. Figure 6 shows the VolcNet data and label for Sierra Negra, as this contains both persistent deformation (inflation prior to the 2018 eruption), and transient deformation (the 2018 eruption).

For the vast majority of time series in the collection, labelling was performed by drawing on the results of previous studies in which inversions had been performed to fit the signals observed in the interferograms, using *Albino et al.* [2019] for Agung, *Xu et al.* [2016] for Wolf, *Gaddes et al.* [2018] for Sierra Negra, *Moore et al.* [2019] for Erta Ale, and *Galetto et al.* [2019] for Cerro Azul. For the remaining time series, labelling was performed through inspection of the signals present. Additionally, several of the studies from which labels were created contain independent validation data in the form of ground truth measurements made using global navigation satellite systems (e.g. Global Positioning System time series are available at Sierra Negra). These data ensure that signals present in time series that are interpreted as being due to physical processes (such as the inflation of a sill or point source) are not actually of atmospheric origin, and are in fact due to deformation of the volcano. However, in some examples assigning a single class to a complex deformation pattern is difficult, and we instead assign what we deem the dominant class to be, whilst expecting that the network should assign some probability to other classes. This is most evident at Wolf, in which signals were attributed to both the deflation of a sill and the opening of a dyke [*Novellis et al.*, 2017; *Xu et al.*, 2016]. Figure 7 details the results of labelling each of these time series, and then creating all possible interferograms between all Sentinel-1 acquisitions.

Figure 8 shows the results of applying our trained classification and localisation model to a quasi-random selection of Sentinel-1 interferograms from the VolcNet database that we define as testing data (i.e. not be used when training models). Interferograms such as Interferogram 8 show a very clear inflation signal at Sierra Negra, and are correctly classified by the CNN ("sill/point"), whilst the localisation is broadly correct. Other promising results include the labelling of the two Wolf coeruptive interferograms (interferograms ten and eleven) as containing a dyke ("sill/point"), which is also localised well. However, some interferograms are wrongly classified, such as the subtle signal seen at Vesuvius (interferogram zero), and the strong atmospheric signals at La Palma (interferogram four), and Campi Flegrei (interferogram two). At Vesuvius, the deformation signal is both small, and surrounded by incoherence and atmospheric signals, and is therefore unlikely to be labelled by a human observer as deformation without inspection of the complete time series. At Campi Flegrei and La Palma, the strong atmospheric signals juxtapose positive and negative signals in a manner somewhat similar to a dyke (our model's label), and this misclassification is likely to be due to our synthetic atmospheric signals not being complex enough to allow our CNN to learn to differentiate between them and deformation. The divergent nature of our CNN's two heads also leads to outputs that show disagreement between them. Interferogram six demonstrates this, in which deformation at Erta Ale is localised approximately but the label is incorrect, although "dyke" has been assigned a probability of 0.48. We again attribute this misclassification to a lack of complexity in our synthetic data limiting what our CNN can learn, as the synthetic dykes we

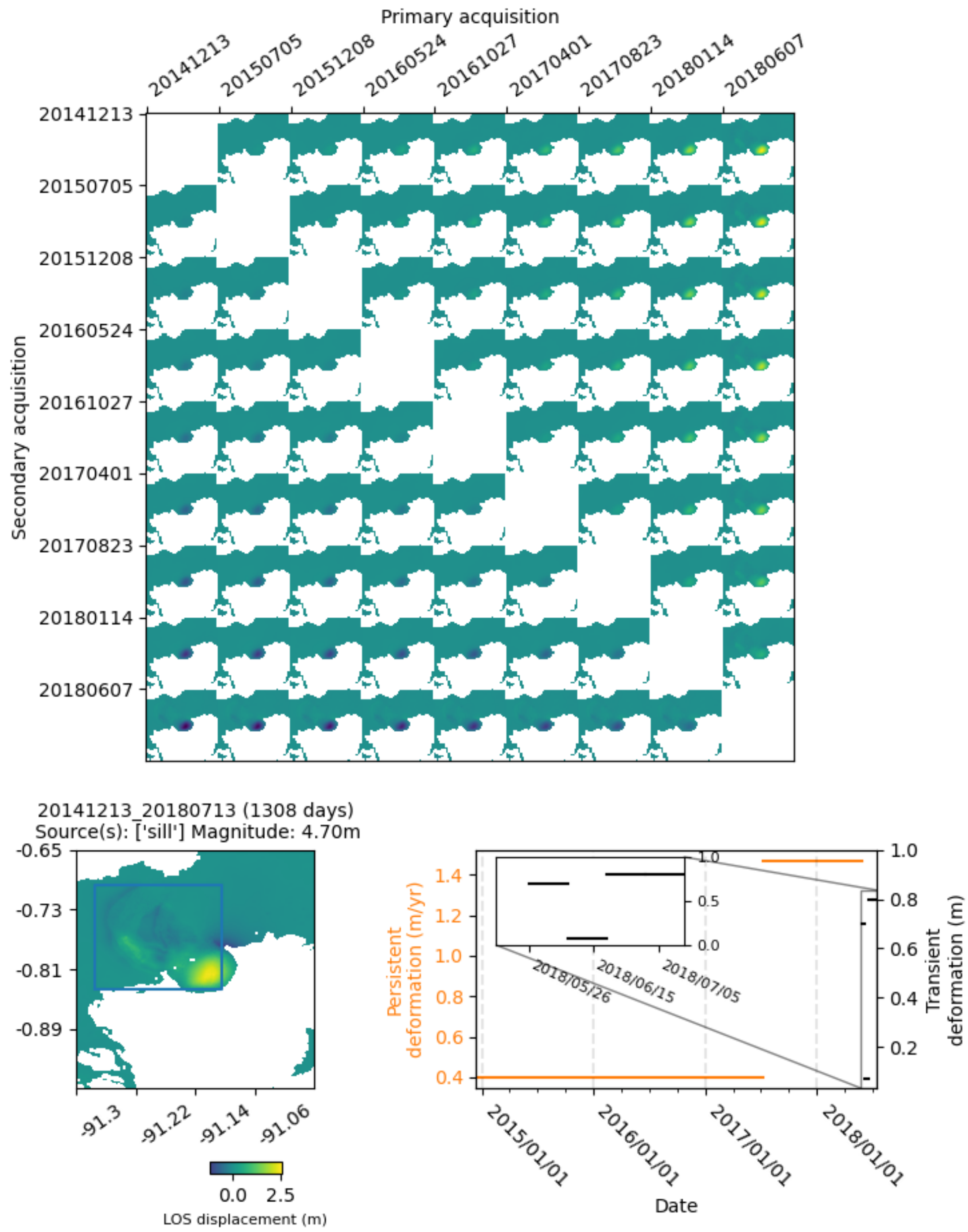

Figure 6. Demonstration of VolcNet labelling for the time series that images Sierra Negra prior to and during the 2018 eruption. Upper: A subset (every 12th) interferogram that can be made between all possible acquisitions, showing the increasing deformation in longer temporal baseline interferograms. Interferograms along the diagonal are omitted as they contain only zeros. Lower left: Example of the longest temporal baseline interferogram that can be created, which features both inflation of the caldera floor (persistent deformation), and complex syneruptive deformation propagating to the north west (transient deformation), for which a single bounding box is automatically created. Lower right: Graphical representation of the labelling, which shows an approximation of the increase in inflation rate that was observed approximately one year before the eruption as an increase in the height of the orange line, and the large but short-lived syneruptive signals in blue.

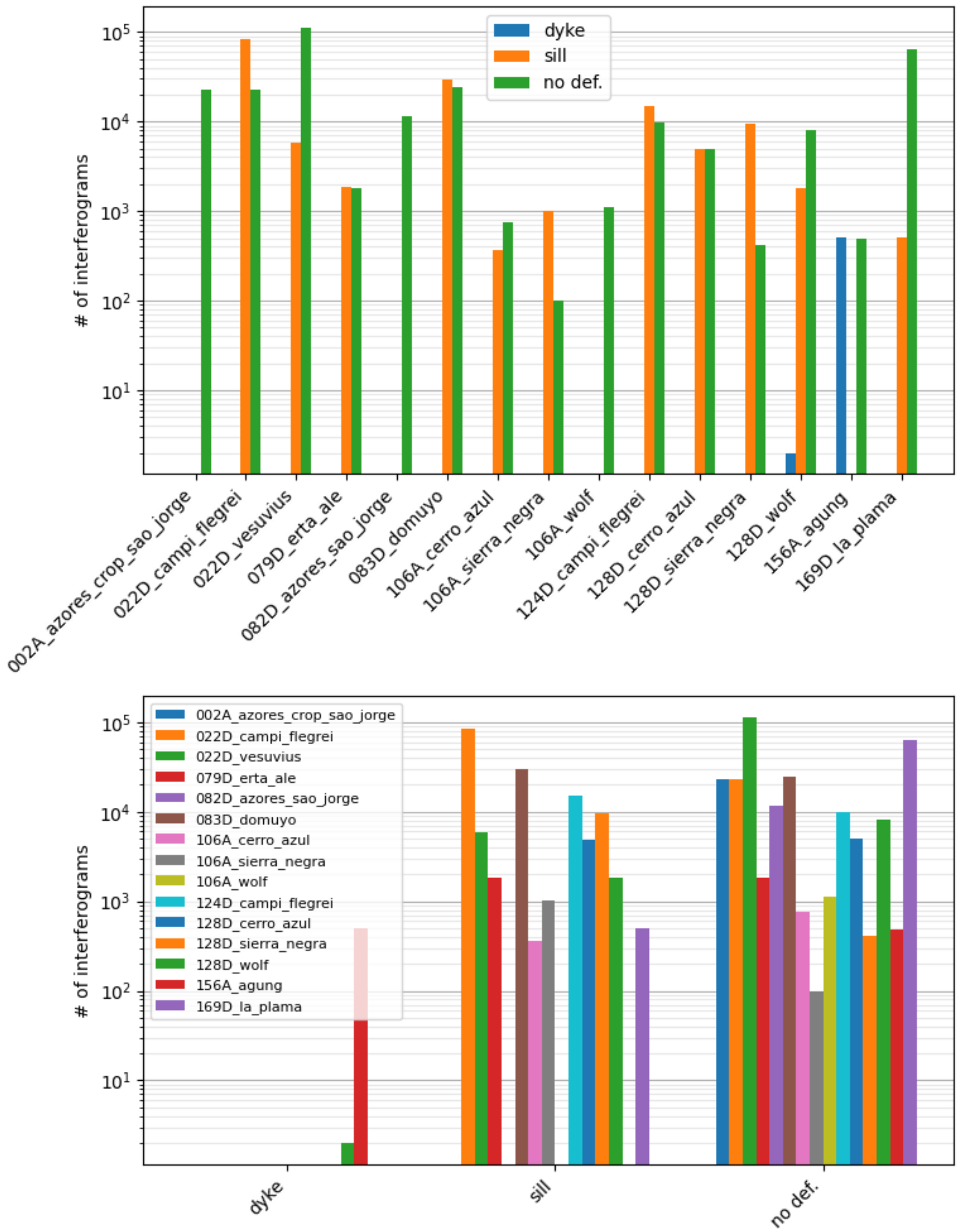

Figure 7. Summary of the VolcNet database. Top: Number of interferograms that can be created at each volcano divided into label type (sill/dyke/no deformation), showing the scarcity of time series that contain deformation attributed to dykes (Agung and Wolf, in blue). Many volcanoes are imaged in both ascending and descending orbits (e.g 128D and 106A for Sierra Negra), and some volcanoes feature in two frames (e.g. 124D and 022D for Campi Flegrei). Bottom: Number of interferograms that can be created of each label type, showing the scarcity of interferograms that contain deformation attributed to a dyke.

use for training (e.g. Figure 2, interferograms two and three) are generally more elongate and less complex than the signal seen at Erta Ale.

3.3 Augmentation of training data with the VolcNet database of Sentinel-1 data

To increase the performance of our model further, we seek to incorporate real Sentinel-1 data from our VolcNet database into the training. Figure 7 details the distribution of labels amongst the fully labelled database, from which the relative scarcity of those labelled as "dyke" can be seen ~500, compared to $\sim 1 \times 10^5$ for "sill" and "no deformation"). This class imbalance in the raw data requires preprocessing to ensure our real training data is as balanced as our synthetic data (i.e. equally), which we achieve through selecting only a random subset of the "sill" and "no deformation" interferograms, resulting in ~1500 labelled interferograms for training and validation use. However, 20000 synthetic interferograms were used to train the previous model, and the inclusion of ~1500 new interferograms is unlikely to impact the model significantly as these could still be classified poorly with minimal increase in the loss function. We therefore apply data augmentation, which involves creating random flips, rotations, and translations of the interferograms to extend our set of real training data to feature 20000 unique, though often highly correlated, Sentinel-1 interferograms. With the exception of including real data, we train our model in the same manner as described in the previous section.

Figure 9 shows the results of applying our CNN to the same test set of real Sentinel-1 VolcNet test interferograms used in Section 3.2. Inspection shows that our model is now better able to handle interferograms with strong atmospheric signals, with interferograms two and four now correctly classified as "no deformation". Localisation is also improved, with visibly smaller errors for interferograms three, and seven. Figure 10 compares the results from the two models across the complete set of VolcNet test data (1000 interferograms), and in all classes both the localisation loss and classification accuracy can be seen to be improved through the incorporation of the real data.

4 Discussion

From the analysis performed in Section 2 we conclude that the incorporation of a DEM into our CNN could not be achieved through the relatively simple step of using it as one channel in multichannel data. This is likely because the weights in the first five con-

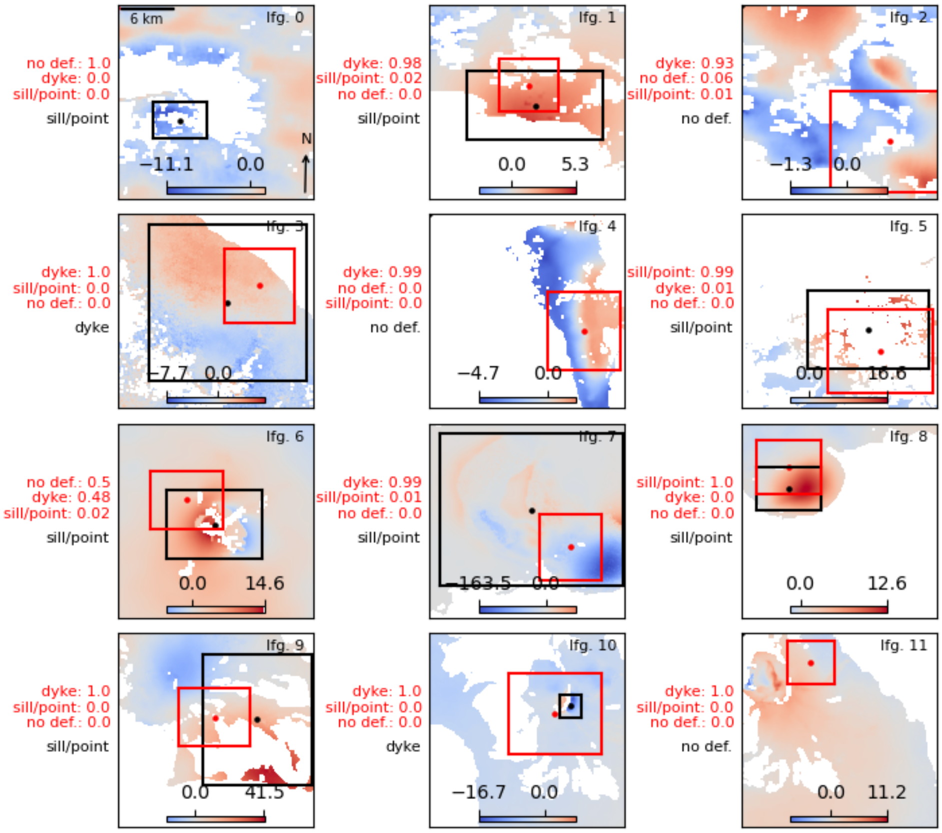

Figure 8. Results of our classification and localisation CNN on our testing set of Sentinel-1 interferograms when the CNN has been trained on synthetic data only. Model predictions are shown in red (including classification probabilities as decimals), and VolcNet labels are shown in black, with deformation shown in centimetres. Interferograms $0:$ Vesuvius, $1 - 2:$ Campi Flegrei, $3:$ Agung, $4:$ La Palma, $5:$ Domuyo, $6:$ Erta Ale, $7 - 8:$ Sierra Negra, $9:$ Cerro Azul, $10 - 11:$ Wolf. Interferograms two and four feature strong atmospheric signals which are misclassified as deformation, and the subtle deformation in zero is misclassified as no deformation. However, in the remaining cases both the classification and localisation is broadly correct, and in 11 the model classification and localisation outperforms the automatic labelling of the VolcNet data as subtle deformation is visible that falls below the threshold for being labelled.

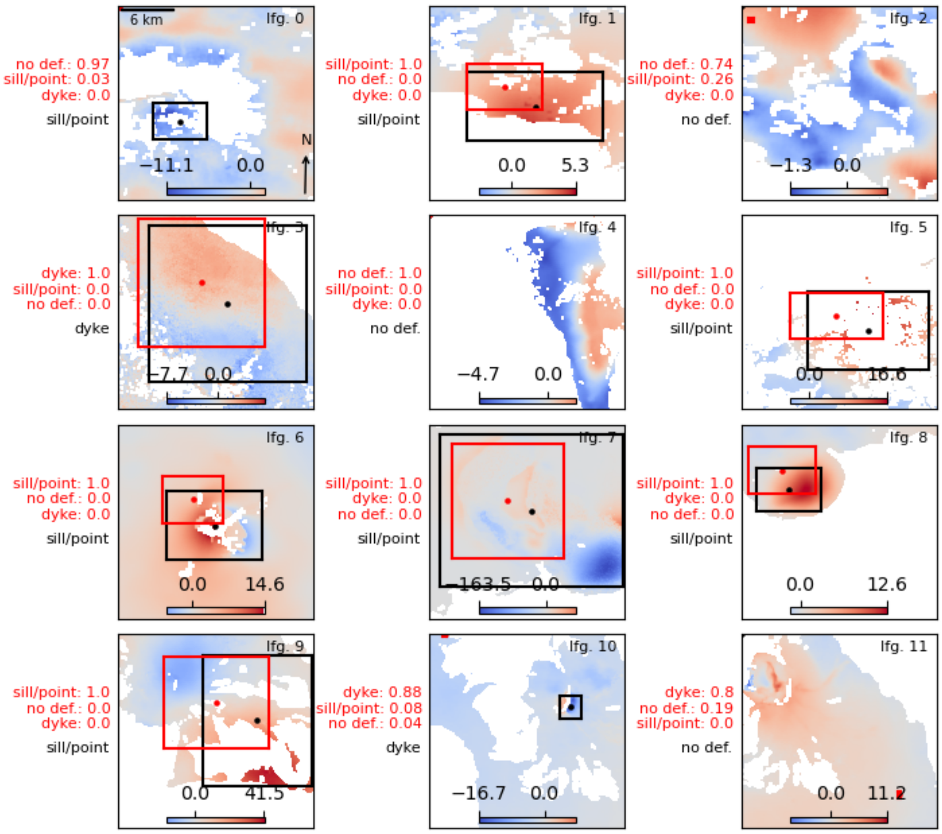

Figure 9. Results of our classification and localisation CNN on our testing set of Sentinel-1 interferograms after incorporating real data into the training. The labelling convention and interferograms are as per Figure 8. This model can be seen to outperform the CNN trained only on synthetic data, with improved classification and localisation in cases such as two and four where strong atmospheric signals are now classed as "no deformation", and seven where the large deformation signal is localised correctly. However, several errors remain, such as the incorrect localisation of a coeruptive Wolf interferogram (10).

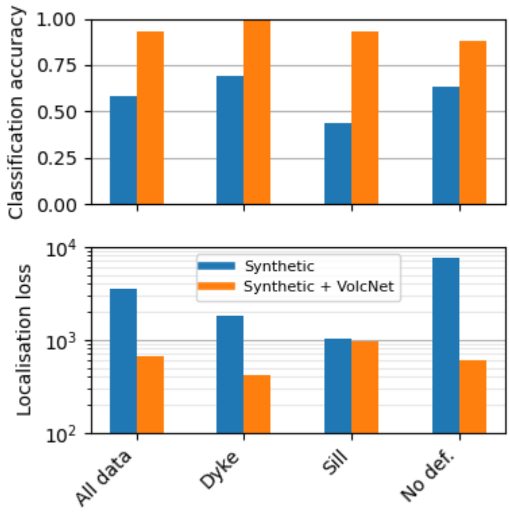

Figure 10. Comparison of the VolcNet test data when evaluated with the model trained with only synthetic data (blue), and with both synthetic and real data (orange). In all cases, the synthetic and real model has both higher classification accuracies, and lower localisation losses than the synthetic only model.

volutional blocks of our model were transferred from VGG16 and, as VGG16 was trained using natural images, inputs which are broadly similar across all three channels are required. It should be noted that we rescaled our training data to lie in the same range as the data that VGG16 was trained on (described further in Section 2), and therefore the lack of similarity across channels we refer to is not due to different magnitudes, but rather, different spatial patterns. However, an approach where the weights within the convolutional blocks of a classification and localisation model were trained from scratch may easily allow for the incorporation of extra data in the different input channels. Whilst this approach was considered during the design of this study, we do not expect that training a CNN from scratch (i.e. training both the convolutional filters and the fully connected network) is feasible with only ~1500 real Sentinel-1 interferograms (i.e. the subset of data in which we balance our three data classes), and we did not have the resources available to create a larger database of labelled data. The results presented in *Sumbul et al.* [2019] explore this theme further, and they find that when using $\sim 600,000$ labelled Sentinel-2 images they are able to train a shallow CNN with a channel for each of Sentinel-2's 13 spectral bands that outperforms a deeper model that was pre-trained using $\sim$ 1.2 million ImageNet images and used only the three visible Sentinel-2 spectral bands. Therefore, we expect that it is likely that through developing the VolcNet database that we introduce in this work (and make freely available to the community), models that are able to use disparate data in the different channels may be trainable, with resulting increases in performance over the model presented here.

However, should the development of a larger training database continue to be problematic, information such as the DEM may be best incorporated through the use of a two input model, in which one set of convolutional filters are applied to the phase information, whilst a second is applied to the DEM. These two networks could then be merged at the fully connected stage, in much the same way as our fully connected model diverges into two outputs. Should this be successful, it may also provide a method to add further inputs to a model, such as those outputted by a weather model, which may reduce false positives due to occurrences such as a strong topographically correlated APS. However, training the weights of a model from scratch and exploring more complex multi-input model architectures remains beyond the remit of this study.

The results presented in Figure 8 show that a model trained only with synthetic data is able to classify and locate deformation signals in Sentinel-1 data. However, it is only successful in cases with particularly clear deformation patterns, and in cases with more subtle signals generally erroneously resorts to labelling these as not containing deformation. Additionaly, strong atmopsheric signals are often misclassified as deformation. It is possible that these limitations may be overcome through the use of more realistic synthetic data, as our result suggests that our current methodology does not describe processes well enough to be used without real data. The generation of more realistic deformation patterns may be achieved through steps such as more intelligent sampling of the parameters used in the forward models used to generate the deformation patterns, the use of different types of deformation models such as penny-shaped cracks [*Fialko et al.*, 2001] or point/Mogi sources [*Mogi*, 1958], and the superposition of multiple deformation patterns in a single interferogram such as was observed prior to the 2005 eruption of Sierra Negra [*Jónsson*, 2009]. The generation of more realistic atmospheric signals could be achieved through increasing the complexity of synthetic data, such as through the use of phase-elevation ratios that are non-linear or spatially variable, or through using data from different sources. Interferograms that image regions with little deformation could be used to increase the complexity of the set of “no deformation" data, or combined with synthetic deformation patterns to produce more complex semi-synthetic data.

The results presented in Figure 9 show the benefit of incorporating real data. However, much scope for improvement remains, with two classification and several localisation errors visible in this figure. The classification error at Vesuvius (interferogram zero) relates to the subtle subsidence signal located near the summit of the volcano, and is so unclear that a human expert would be unlikely to label this as deformation without further analysis (e.g. inspecting the complete time series). The classification error at Wolf (interferogram 11) is more complex, and on inspection suggests that the error is caused by the incorrect labelling of the interferogram during its construction from the VolcNet database, and that our CNN is actually correct. This is likely to be a consequence of how we determine a minimum threshold of deformation in an interferogram for it to be labelled as “deformation”, and serves to illustrate a potential disadvantage of our automatic labelling approach. The majority of the localisation errors are in the form of inaccuracy relating to the centre of the deformation or its spatial size, and from this we conclude that our localisation head may not be complex enough to capture the large variety possible in both the location and spatial extend of a signal. Further refinement of this part of the model lies outside the scope of this paper, but is not likely to be addressed through incremental improvements to the fully connected head, but rather through complete replacement with a more complex model such as R-CNN [*Girshick et al.*, 2013]. The training of more complex models is likely to require more real data from the VolcNet database, which may be addressed through incorporating more time series, and by addressing the large disparity in the number of data per class (i.e. the scarcity of dykes) that limits the number of other interferograms that we are able to use in this study.

The divergent nature of the two heads (classification and localisation) of our network also allows for discrepancies between their outputs. This is seen in interferogram 10 of Figure 9, in which the localisation head produces a broadly correct output, but the signal is incorrectly labelled as “no deformation", although with a relatively low confidence. However, we postulate that it may be possible to avoid errors of this type by using more complex model architectures. Models such as YOLO [*Redmon et al.*, 2016] produce bounding boxes and classifications in one step, and have the added bonus of being able to work with images that contain multiple signals. If successfully applied to interferograms, a model of this complexity may avoid the discrepancy errors we encounter, and be able to handle interferograms that contain multiple deformation patterns. In the case that multiple signals do exist in a single interferogram, we do not envisage these to be difficult to label as it is likely that these would be considered interesting events by the scientific community and therefore be the subject of detailed study (e.g. the multi-signal interferograms used in this study are analysed in detail in [*Xu et al.*, 2016]).

Our approach to localisation avoids the need for repeated classification using a sliding window approach, and allows for our network to reason using the entire image. Whilst this approach is beneficial in terms of advancing the state-of-the-art towards that of a human interpreter, one caveat remains in that building a network that is able to utilise large interferograms can be complex. In our model, we use pixels of three arc second size and, with an input size of 224×224, the resulting model is able to "see" an approximately 20km square around a volcano. If we wish to proceed at this resolution, our model's visual field could be increased through changing the input size to around 400×400 which would not impact our ability to use VGG16's filters (or convolutional blocks), but would increase the size of the first layer of the fully connected part of our network.

At present, an input with side length 224 is reduced to a feature map with side length 7 (shown in Figure 4) which, combined with a depth of 512, produces a flattened layer of size $7 \times 7 \times 512 = 25088$. However, doubling the input side length would double the feature map side length, increasing the flattened layer to a size of $14 \times 14 \times 512 = 100352$. Whist our model contains millions of free parameters, connecting this layer to a subsequent layer would produce a significant increase in the total, and is likely to require either more ingenuity or more data to be trained successfully. Analysis of the offsets of deformation patterns at volcanic centres by *Ebmeier et al.* [2018] finds that 8% of signals are located more than 10km from a volcanic edifice, and would therefore be missed by our current model. Future models that wish to perform localisation using a global approach may therefore require slight increases in size in order to capture all signals of interest. Alternatively, as per the approach of [*Anantrasirichai et al.*, 2018], CNNs can themselves be convolved across larger images (such as those routinely captured by the TOPSAR mode of the Sentinel-1 satellites) to create repeat classifications, and this may provide a way to apply our current model to images for which the number of parameters in the first layer of the fully connected network is prohibitive. However, for application to large scenes that capture non-volcanic deformation, a network similar to the fully convolutional network (FCN) presented in *Rouet-Leduc et al.* [2020] may be more suitable, as this contains no fully connected network and so can be applied to an input of near arbitrary size.

The smallest deformation signals that our model can accurately label are of approximately 5 cm in magnitude, which is a product of us choosing this threshold as the minimum deformation required for a VolcNet interferogram to be considered as containing deformation. A benefit of our novel labelling approach is that through decreasing this parameter, we can produce single interferograms that span persistent deformation that is not visible to the human observer (e.g. 1 cm of deformation is not likely to be visible through the atmospheric noise of several to tens of centimetres commonly encountered at volcanoes). Relabelling the VolcNet database could therefore be done at increasingly lower deformation thresholds, and provide a route to train deep learning models that outperform human domain experts. Through computing cumulative displacements in the manner described in *Anantrasirichai et al.* [2019b], our existing method could also be extended to extremely low rate signals, providing a long enough time series is present.

In addition to making our VolcNet database available via GitHub, we make all the code for training our two deep learning models (VUDL-NET-21: "Volcanic Unrest Detection and Localisation NET, 2021") available on GitHub: (https://github.com/matthew-gaddes/VUDLNet_21)

5 Conclusion

We find that either wrapped or unwrapped data are approximately equally suited for use with the weights of VGG16's filters trained on ImageNet data. We also find that incorporating extra information that a human interpreter may use (such as a DEM) in the two otherwise unused channels of a model trained in this way acts to degrade model performance, and we postulate that this is a result of the disparate nature of the signals contained within a DEM and the phase of an interferogram. However, we expect this will not be the case if the weights within VGG16's filters are trained from scratch, as additional data such as a DEM should help to separate deformation from noise.

We combine the five convolutional blocks of VGG16 with two fully connected networks to perform both classification and localisation of deformation, which allows our network to reason using the whole interferogram (i.e. avoiding a sliding window approach), and therefore move a step closer to interpreting InSAR data in a manner similar to a human expert. Additionally, our network is able to differentiate between several different forms of deformation, and advances the state-of-the-art. We expect that further work may build on the results presented in this manuscript and use the same method to increase the number of deformation signals that a model is able to identify. For use with volcano monitoring, this may include models that are able to classify signals such as those due to cooling lava flows, or those due to unstable volcano flanks. For use in the broader remote sensing community, this three class model could be adapted to perform tasks such as differentiating between strike-slip, thrust, and normal fault earthquakes in single interferograms.

As Sentinel-1 interferograms are being automatically created for the majority of the world's subaerial volcanoes every 6 or 12 days, our algorithm provides a method to search through this vast and regularly changing database to search for signs of deformation that may indicate that a volcano has entered a period of unrest. Through doing this, the algorithm could facilitate monitoring of many currently unmonitored volcanoes. Additionally, as our model is able to localise any deformation it does encounter, this allows the model to determine the spatial extent of a signal (i.e. the area of the bounding box it creates), and so provide information that is likely to be useful when determining how urgently interferograms that it flags should be inspected by a human expert.

To minimise the costly nature of labelling data, we initially train our model using only synthetic data. We find that our model generalises well to some cases of Sentinel-1 data, but errors remain in cases such as subtle deformation signals, or unusual atmospheric signals. We alleviate this problem through building a database of Sentinel-1 data, which we term VolcNet, that uses a novel labelling strategy to create $\sim 500,000$ labelled interferograms from relatively few labels. The inclusion of a small amount of this real data during the training phase improves model performance drastically, and we present a model that is able to both classify and locate deformation within interferograms of ~20km side length. For other practitioners seeking to train similar models, we make both our code for generating synthetic interferograms (SyInterferoPy), our labelled Sentinel-1 data (VolcNet), and our two models (VUDL-NET21) freely available via GitHub.

Acknowledgments

This work was supported by the NERC Centre for the Observation and Modelling of Earthquakes, Volcanoes and Tectonics (COMET). M. E. G. was supported by the Natural Environment Research Council (NERC) grant Looking Inside Continents from Space (LiCS, NE/ K011006/1), and by a European Space Agency Living Planet Fellowship. This project has received funding from the European Research Council (ERC) through the EU Horizon 2020 project DEEPVOLC (grant number 866085). The Copernicus Sentinel data were acquired by the European Space Agency (ESA) and were obtained by the authors of this study from the Alaska Satellite Facility archive (https://www.asf.alaska.edu/). Figures were prepared in Matplotlib [*Hunter*, 2007], and all CNN work was carried out in KERAS using the TensorFlow backend.

References

Agostinelli, F., M. Hoffman, P. Sadowski, and P. Baldi (2014), Learning activation functions to improve deep neural networks, *arXiv preprint arXiv:1412.6830*.

Albino, F., J. Biggs, and D. K. Syahbana (2019), Dyke intrusion between neighbouring arc volcanoes responsible for 2017 pre-eruptive seismic swarm at agung, *Nature communications*, *10*(1), 1–11.

Albino, F., J. Biggs, C. Yu, and Z. Li (2020), Automated methods for detecting volcanic deformation using sentinel-1 insar time series illustrated by the 2017–2018 unrest at agung, indonesia, *Journal of Geophysical Research: Solid Earth*, *125*(2), e2019JB017,908.

Anantrasirichai, N., J. Biggs, F. Albino, P. Hill, and D. Bull (2018), Application of Machine Learning to Classification of Volcanic Deformation in Routinely Generated InSAR Data, *Journal of Geophysical Research : Solid Earth*, pp. 1–15, doi: 10.1029/2018JB015911.

Anantrasirichai, N., J. Biggs, F. Albino, and D. Bull (2019a), A deep learning approach to detecting volcano deformation from satellite imagery using synthetic datasets, *RSE*, pp. 1–15, doi:10.1029/2018JB015911.

Anantrasirichai, N., J. Biggs, F. Albino, and D. Bull (2019b), The application of convolutional neural networks to detect slow, sustained deformation in insar time series, *Geophysical Research Letters*, *46*(21), 11,850–11,858.

Beauducel, F., P. Briole, and J.-L. Froger (2000), Volcano-wide fringes in ers synthetic aperture radar interferograms of etna (1992–1998): Deformation or tropospheric effect?, *Journal of Geophysical Research: Solid Earth*, *105*(B7), 16,391–16,402.

Biggs, J., S. K. Ebmeier, W. P. Aspinall, Z. Lu, M. E. Pritchard, R. S. J. Sparks, and T. a. Mather (2014), Global link between deformation and volcanic eruption quantified by satellite imagery., *Nature communications*, *5*, 3471, doi:10.1038/ncomms4471.

Bountos, N. I., I. Papoutsis, D. Michail, A. Karavias, P. Elias, and I. Parcharidis (2022), Hephaestus: A large scale multitask dataset towards insar understanding, in *Proceedings of the IEEE/CVF Conference on Computer Vision and Pattern Recognition*, pp. 1453–1462.

Bridle, J. S. (1990), Probabilistic interpretation of feedforward classification network outputs, with relationships to statistical pattern recognition, in *Neurocomputing*, pp. 227–236, Springer.

Chen, C. W., and H. A. Zebker (2001), Two-dimensional phase unwrapping with use of statistical models for cost functions in nonlinear optimization, *Journal of the Optical Society of America*, *18*(2), 338–351.

Chollet, F. (2017), *Deep learning with Python*, Simon and Schuster.

Deng, J., W. Dong, R. Socher, L.-J. Li, K. Li, and L. Fei-Fei (2009), Imagenet: A large-scale hierarchical image database, in *Computer Vision and Pattern Recognition, 2009. CVPR 2009. IEEE Conference on*, pp. 248–255, Ieee.

Dozat, T. (2016), Incorporating nesterov momentum into adam.

Ebmeier, S. K., B. J. Andrews, M. C. Araya, D. W. D. Arnold, J. Biggs, C. Cooper, E. Cottrell, M. Furtney, J. Hickey, J. Jay, R. Lloyd, A. L. Parker, M. E. Pritchard, E. Robertson, E. Venzke, and J. L. Williamson (2018), Synthesis of global satellite observations of magmatic and volcanic deformation : implications for volcano monitoring & the lateral extent of magmatic domains, *Journal of Applied Volcanology*, pp. 1–26, doi:10.1186/s13617-018-0071-3.

Farr, T., P. Rosen, E. Caro, and R. Crippen (2007), The Shuttle Radar Topography Mission, *Reviews of Geophysics*, *45*(2005), 1–33, doi:10.1029/2005RG000183.1.

Fialko, Y., Y. Khazan, and M. Simons (2001), Deformation due to a pressurized horizontal circular crake in an elastic half-space, with application to volcano geodesy, *Geophys. J. Int.*, *146*, 181–190.

Gaddes, M., A. Hooper, M. Bagnardi, H. Inman, and F. Albino (2018), Blind signal separation methods for insar: The potential to automatically detect and monitor signals of volcanic deformation, *Journal of Geophysical Research: Solid Earth*.

Galetto, F., M. Bagnardi, V. Acocella, and A. Hooper (2019), Noneruptive unrest at the caldera of alcedo volcano (galápagos islands) revealed by insar data and geodetic modeling, *Journal of Geophysical Research: Solid Earth*, *124*(4), 3365–3381.

Girshick, R. B., J. Donahue, T. Darrell, and J. Malik (2013), Rich feature hierarchies for accurate object detection and semantic segmentation, *CoRR*, *abs/1311.2524*.

Goldstein, R. M., and C. L. Werner (1998), Radar interferogram filtering for geophysical applications, *Geophysical Research Letters*, *25*(21), 4035, doi:10.1029/1998GL900033.

Hanssen, R. F. (2001), *Radar interferometry: data interpretation and error analysis*, vol. 2, Springer Science & Business Media.

He, K., X. Zhang, S. Ren, and J. Sun (2016), Deep residual learning for image recognition, in *Proceedings of the IEEE conference on computer vision and pattern recognition*, pp. 770–778.

He, K., G. Gkioxari, P. Dollár, and R. Girshick (2017), Mask r-cnn, in *Proceedings of the IEEE international conference on computer vision*, pp. 2961–2969.

Hunter, J. D. (2007), Matplotlib: A 2d graphics environment, *Computing In Science & Engineering*, *9*(3), 90–95.

Jónsson, S. (2009), Stress interaction between magma accumulation and trapdoor faulting on Sierra Negra volcano, Galápagos, *Tectonophysics*, *471*(1-2), 36–44, doi:10.1016/j.tecto.2008.08.005.

Kingma, D. P., and J. Ba (2014), Adam: A method for stochastic optimization, *arXiv preprint arXiv:1412.6980*.

Krizhevsky, A., I. Sutskever, and G. E. Hinton (2012), Imagenet classification with deep convolutional neural networks, in *Advances in neural information processing systems*, pp. 1097–1105.

Lazeckỳ, M., K. Spaans, P. J. González, Y. Maghsoudi, Y. Morishita, F. Albino, J. Elliott, N. Greenall, E. Hatton, A. Hooper, et al. (2020), Licsar: An automatic insar tool for measuring and monitoring tectonic and volcanic activity, *Remote Sensing*, *12*(15), 2430.

Mogi, K. (1958), Relations between the eruptions of various volcanoes and the deformations of the ground surfaces around them, *Bulletin of the Earthquake Research Institute*, *36*, 99–134, doi:10.1016/j.epsl.2004.04.016.

Moore, C., T. Wright, A. Hooper, and J. Biggs (2019), The 2017 eruption of erta'ale volcano, ethiopia: Insights into the shallow axial plumbing system of an incipient mid-ocean ridge, *Geochemistry, Geophysics, Geosystems*, *20*(12), 5727–5743.

Morishita, Y., M. Lazecky, T. J. Wright, J. R. Weiss, J. R. Elliott, and A. Hooper (2020), Licsbas: an open-source insar time series analysis package integrated with the licsar automated sentinel-1 insar processor, *Remote Sensing*, *12*(3), 424.

Novellis, V. D., R. Castaldo, C. D. Luca, S. Pepe, I. Zinno, F. Casu, R. Lanari, and G. Solaro (2017), Source modelling of the 2015 Wolf volcano (Galápagos) eruption inferred from Sentinel 1-A DInSAR deformation maps and pre-eruptive ENVISAT time series, *Journal of Volcanology and Geothermal Research*, *344*, 246–256, doi: 10.1016/j.jvolgeores.2017.05.013.

Okada (1985), Surface deformation due to shear and tensile faults in a half-space, *International Journal of Rock Mechanics and Mining Sciences Geomechanics Abstracts*, *75*(4), 1135–1154, doi:10.1016/0148-9062(86)90674-1.

Redmon, J., S. Divvala, R. Girshick, and A. Farhadi (2016), You only look once: Unified, real-time object detection, in *Proceedings of the IEEE conference on computer vision and pattern recognition*, pp. 779–788.

Rémy, D., Y. Chen, J.-L. Froger, S. Bonvalot, L. Cordoba, and J. Fustos (2015), Revised interpretation of recent insar signals observed at llaima volcano (chile), *Geophysical Research Letters*, *42*(10), 3870–3879.

Ronneberger, O., P. Fischer, and T. Brox (2015), U-net: Convolutional networks for biomedical image segmentation, in *International Conference on Medical image computing and computer-assisted intervention*, pp. 234–241, Springer.

Rouet-Leduc, B., R. Jolivet, M. Dalaison, P. A. Johnson, and C. Hulbert (2020), Autonomous extraction of millimeter-scale deformation in insar time series using deep learning, *arXiv preprint arXiv:2012.13849*.

Simonyan, K., and A. Zisserman (2014), Very deep convolutional networks for large-scale image recognition, *arXiv preprint arXiv:1409.1556*.

Srivastava, N., G. Hinton, A. Krizhevsky, I. Sutskever, and R. Salakhutdinov (2014), Dropout: a simple way to prevent neural networks from overfitting, *The Journal of Machine Learning Research*, *15*(1), 1929–1958.

Sumbul, G., M. Charfuelan, B. Demir, and V. Markl (2019), Bigearthnet: A large-scale benchmark archive for remote sensing image understanding, *arXiv preprint arXiv:1902.06148*.

Sun, J., C. Wauthier, K. Stephens, M. Gervais, G. Cervone, P. La Femina, and M. Higgins (2020), Automatic detection of volcanic surface deformation using deep learning, *Journal of Geophysical Research: Solid Earth*, *125*(9), e2020JB019,840.

Szegedy, C., W. Liu, Y. Jia, P. Sermanet, S. Reed, D. Anguelov, D. Erhan, V. Vanhoucke, and A. Rabinovich (2015), Going deeper with convolutions, in *Proceedings of the IEEE* *conference on computer vision and pattern recognition*, pp. 1–9.

Valade, S., A. Ley, F. Massimetti, O. DâĂŹHondt, M. Laiolo, D. Coppola, D. Loibl, O. Hellwich, and T. R. Walter (2019), Towards global volcano monitoring using multisensor sentinel missions and artificial intelligence: The mounts monitoring system, *Remote Sensing*, *11*(13), 1528.

Xu, W., S. Jónsson, J. Ruch, and Y. Aoki (2016), The 2015 Wolf volcano (Galápagos) eruption studied using Sentinel-1 and ALOS-2 data, *Geophysical Research Letters*, pp. 9573–9580, doi:10.1002/2016GL069820.

Yip, S. T. H., J. Biggs, and F. Albino (2019), Reevaluating volcanic deformation using atmospheric corrections: Implications for the magmatic system of agung volcano, indonesia, *Geophysical Research Letters*, *46*(23), 13,704–13,711.

Yu, D., and M. L. Seltzer (2011), Improved bottleneck features using pretrained deep neural networks, in *Twelfth annual conference of the international speech communication association*.

Zhang, Q., Y. Wang, Q. Liu, X. Liu, and W. Wang (2016), Cnn based suburban building detection using monocular high resolution google earth images, in *2016 IEEE International Geoscience and Remote Sensing Symposium (IGARSS)*, pp. 661–664, IEEE.